

Cite this: *J. Mater. Chem. C*, 2017, 5, 10114Received 29th June 2017,
Accepted 15th September 2017

DOI: 10.1039/c7tc02928d

rsc.li/materials-c

Tailoring nucleation and grain growth by changing the precursor phase ratio for efficient organic lead halide perovskite optoelectronic devices†

Swaminathan Venkatesan,[‡] Mehedhi Hasan,^{ib} Junyoung Kim,^{ib} Nader R. Rady,^a Sandeep Sohal,^{ib} Eric Neier,^a Yan Yao^{ib} and Alex Zakhidov^{*ab}

The nucleation and growth of organic–inorganic hybrid perovskite films induced by the molar ratio of precursor components and their role in optoelectronic performance are investigated. Lead iodide (PbI₂), methylammonium acetate (MAAc) and methylammonium iodide (MAI) mixed in different ratios were used as starting precursors for active layer deposition. While all the as cast films showed the presence of a precursor intermediate (PbI_x-MAAc-MAI), the films derived from 1:1:1 and 1:0.5:1 ratios also exhibited crystallization of the perovskite (CH₃NH₃PbI₃) phase during the spin coating process. The nucleation and crystallization of the perovskite phase in films derived from the equimolar precursor ratio were found to be the key to growing larger, smoother and single crystalline grains along the thickness leading to higher carrier lifetimes. Perovskite solar cells fabricated utilizing such a morphology showed a much higher power conversion efficiency irrespective of the active layer thickness. Furthermore, methyl ammonium bromide based perovskite light emitting diodes were also fabricated using the aforementioned equimolar precursor ratio which exhibited superior device performance compared to diodes with active layers derived from other precursor ratios. This work highlights a facile deposition technique and growth mechanism to attain reproducible, low cost and high-performance perovskite optoelectronic devices.

Introduction

Organic–inorganic trihalide hybrid perovskite (OTP) materials have gained recent attention due to their low cost and superior optoelectronic properties such as high absorption coefficient,

carrier diffusion lengths, long carrier lifetimes, *etc.* These OTP materials which have the chemical formula MAPbX₃ are typically obtained by the reaction between organic salts namely methylammonium salt (MAX) and lead salt (PbX₂) where X is I, Br or Cl. However, due to the rapid reaction kinetics, often the resulting morphology of films coated with a mixture of two salts is rough and not suitable for thin film devices. To overcome this issue researchers have either used an approach of intermediates using lead halide adducts or a sequential coating technique of each salt.^{1,2} Although both of these approaches have resulted in spectacular device performances, these methods are not ideal for large scale coating due to several reasons. The single step intermediate phase approach requires the films to be washed with an orthogonal solvent or a gas flush prior to thermal annealing.³ The orthogonal solvent washing leads to quenching of the lead halide-solvent adduct which forms a uniform film and upon annealing the induced phase transformation gives rise to a desired smooth film morphology and coverage. While this is easily achieved on smaller scale substrates with spin coating methods, it poses serious challenges for larger scale coating methods such as roll-to-roll or slot-die coating. On the other hand, two step approaches need meticulous and careful optimization as the conditions for both steps are interdependent. Ideally for roll-to-roll coating a single solvent with low viscosity is needed with minimal post processing steps to enable cost effectiveness and high throughput.⁴

To achieve a simple and scalable coating, perovskites derived from a non-halogenated lead source namely lead acetate (Pb(Ac)₂) are shown to be effective. A perovskite film coated with Pb(Ac)₂ possesses uniform coverage and smooth morphology nullifying the requirement for any additional quenching process.⁵ In spite of the advantages of smooth film formation, coverage and quick conversion, the grain growth from Pb(Ac)₂ has shown to be the limiting factor for efficient photovoltaic devices. This is due to the fact that nucleation and grain growth of CH₃NH₃PbI₃ from the Pb(Ac)₂ precursor occur very fast and at low annealing temperatures, which leads to

^a Department of Physics, Texas State University, San Marcos, TX, 78666, USA.
E-mail: alex.zakhidov@txstate.edu

^b Materials Science Engineering and Commercialization, Texas State University, San Marcos, TX, 78666, USA

^c Department of Electrical and Computer Engineering, University of Houston, Houston, TX, 77204, USA

† Electronic supplementary information (ESI) available. See DOI: 10.1039/c7tc02928d

‡ These authors contributed equally.

smaller grains and defective interfaces.⁶ Often researchers have used alternative methods such as inclusion of additives,⁷ lead chloride,⁸ ambient exposure, Ostwald ripening⁹ and solvent annealing¹⁰ to enhance the grain size and lower the defects. Particularly in our previous study, we have shown that the nucleation of the perovskite phase can be achieved by exposing the as deposited $\text{Pb}(\text{Ac})_2$:MAI films prior to thermal annealing.¹¹ Such an ambient exposure leads to substantial reduction in trap densities and charge transport barriers thereby eventually enhancing the photovoltaic performance. Similarly, a study by Dubey *et al.* shows that solvent quenched intermediate films exposed to ambient air led to a slow conversion of the intermediate phase to the perovskite phase.¹² This slow conversion in ambient air led to the ideal morphology of perovskite films possessing improved optical and charge transport properties compared to films annealed in nitrogen. Highlighting the significance of nucleation, Grätzel and coworkers obtained above 21% power conversion efficiency by utilizing poly(methyl methacrylate) (PMMA) templated growth of perovskite solar cells.¹³ It is critical to understand the compositional induced perovskite nucleation and grain growth mechanism to realize optimal ink formulations and enable quick conversion to high-quality perovskites. Such an insight will be of importance for scaling up for large area and roll-to-roll coating technologies.

In this communication, we report the role of the precursor mixing ratios, specifically the ratio between the lead salt (PbX_2) and methylammonium acetate (MAAc) in nucleation and grain growth of perovskites. It is observed that the precursor solutions with equivalent and deficient molar ratios of MAAc relative to PbX_2 enable nucleation of the perovskite phase during spin coating. Such a deposition induced nucleation led to the growth of larger perovskite grains with a lower defect density resulting in efficient photovoltaic and light emitting devices. This approach enables a facile single step route to grow high-quality perovskite films for low cost and high-performance optoelectronic devices.

Results and discussion

Fig. 1a shows photographs of the as cast films derived from different precursor ratios of PbI_2 :MAAc:MAI. MAAc was synthesized by the reaction of anhydrous methylamine (MA) gas and acetic acid, and the formed salt was precipitated in toluene. Further details of the synthesis can be found in the Experimental section. MAAc acts merely as a byproduct in the formation of MAPbI_3 , and its ratio was varied. The molar ratio of PbI_2 and MAI was kept stoichiometric (*i.e.* 1:1) for all precursor solutions with different MAAc ratios. The films with 1:2:1 PbI_2 :MAAc:MAI possessed yellow color as observed for the films coated with a 1:3 molar ratio of $\text{Pb}(\text{Ac})_2$:MAI which is the conventional mixing ratio for perovskites derived from the $\text{Pb}(\text{Ac})_2$ based precursor. Similarly, 1:1:1 PbI_2 :MAAc:MAI precursors can be formulated from 0.5:0.5:2 molar ratios of PbI_2 : $\text{Pb}(\text{Ac})_2$:MAI. The films coated with 1:1:1 precursor ratios were specular dark brown colored and the transition in the color occurred during the process of spin coating. The transition in the film color from

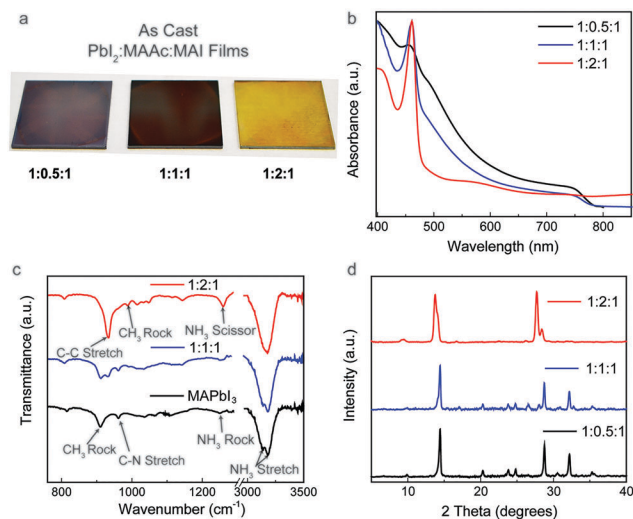


Fig. 1 (a) Optical photographs of the as cast films, (b) Fourier transform infrared spectroscopy (FTIR), (c) UV-visible absorption spectra and (d) X-ray diffraction (XRD) patterns of the as deposited PbI_2 :MAAc:MAI films mixed in different molar ratios.

transparent to dark brown was also noticed for films coated with a 1:0.5:1 precursor ratio, however, these films were darker and had a whitish tint. This whitish tint arose from the light scattering film possibly due to the rougher morphology. Films derived from very low or no precursor MAAc molar ratios turned out to be light brownish in color with a quite rough morphology and incomplete surface coverage similar to those obtained with MAI and PbI_2 solution in DMF.¹⁴ In order to understand the optical transitions, UV-Visible absorption spectra for all the as cast films were measured and are shown in Fig. 1b. For all the films, an excitonic absorption peak is observed at 460 nm. Such excitonic optical transitions are attributed to charge transfer in plumbate complexes¹⁵ and low dimensional perovskites.¹⁴ In our previous study, we have shown that this absorption peak belongs to the PbI_x -MAAc-MAI intermediate phase.¹¹ While all films show this excitonic peak, a brown color in 1:1:1 and 1:0.5:1 is formed from the onset of absorption at 770 nm indicative of the formation of the perovskite phase. The higher absorbance in 1:0.5:1 films compared to the absorbance of 1:1:1 films is attributed to the higher composition of the perovskite phase formation in the 1:0.5:1 films as evident from the XRD discussed below. This perovskite phase formation is also observed in the FTIR spectra of the as deposited 1:1:1 films shown in Fig. 1c. FTIR transmittance spectra of 1:2:1 films show peaks at 935 cm^{-1} , 988 cm^{-1} and 1258 cm^{-1} characteristic of C-C stretch, CH_3 rock and NH_3 scissor of an acetate functional group respectively. FTIR spectra of 1:1:1 films show peaks similar to that of acetate along with certain characteristic peaks of the perovskite phase namely CH_3 rock (911 cm^{-1}), C-N stretch (960 cm^{-1}) and NH_3 stretch (3132 cm^{-1} and 3170 cm^{-1}) of MAPbI_3 .¹⁶ Hence it is evident that in 1:1:1 films crystallization of the perovskite phase occurs during spin coating and in the case of 1:2:1 films the predominant phase is the PbI_x -MAAc-MAI intermediate. Fig. 1d shows the XRD pattern of the as

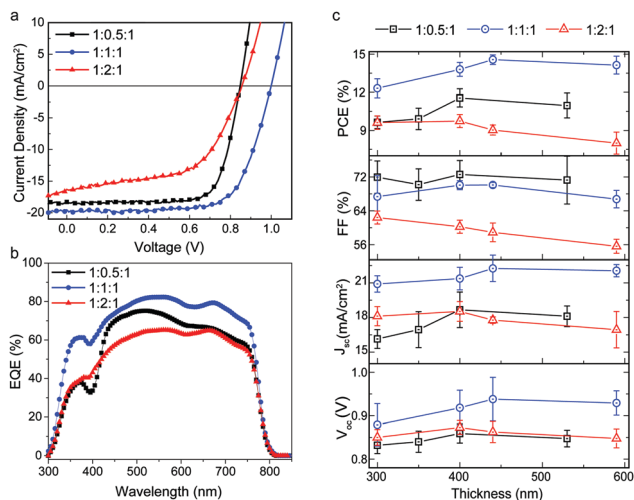


Fig. 2 (a) Current density vs. voltage plot of solar cells, (b) external quantum efficiency (EQE) and (c) photovoltaic parameters vs. thickness of perovskite solar cells derived from different precursor ratios.

deposited films of three different mixing ratios. The peak below 10° at 9.5° belongs to the intermediate of $\text{PbI}_x\text{-MAI-MAAc}$ as shown in our previous study. The exact composition and structure are not known yet and still need to be elucidated. The films derived from all three precursor ratios show peaks at $\sim 14^\circ$ and $\sim 28^\circ$ representative of perovskite crystal orientations (002)/(110) and (004)/(220) respectively. A closer look at these peaks reveals that 1:2:1 films show a more dominant cubic phase (002) peak at 13.76° and a smaller (110) shoulder at 14.12° .¹⁷ This difference is easily observable in the second order peak of each, namely (004) at 27.7° and (220) at 28.46° . While the (110) and (220) peaks are also present in films coated with 1:1:1 precursor ratios, the preferred growth is still along the (110) crystallographic orientation. Growth along the (110) direction has been shown to be favorable for less defective grains by Li *et al.*¹⁸ where the study highlights the role of inorganic seeding agents for the preferred crystal orientation.

Fig. 2a shows the current density–voltage plots of solar cells fabricated with perovskite active layers derived from different precursor ratios. The active layer thickness for the representative cells was ~ 500 nm. The photovoltaic parameters are tabulated in Table 1. Among all devices, solar cells with 1:2:1 active layers showed the poorest power conversion efficiency (PCE) of 8.11% with an open circuit voltage (V_{oc}) of 0.856 V, a short circuit current density (J_{sc}) of 16.31 mA cm^{-2} and a fill factor (FF) of 58.08. The devices with 1:1:1 ratios showed the best performance with a PCE of 15.00% with a V_{oc} of 1.002 V, a J_{sc} of 21.66 mA cm^{-2} and a FF of 69.11. Devices with 1:0.5:1 active layers showed a mediocre PCE of 11.74% with a V_{oc} of 0.847 V, a

J_{sc} of 18.29 mA cm^{-2} and the highest FF of 75.69. The improved PCE in 1:1:1 and 1:0.5:1 devices arises mainly due to an increase in the J_{sc} and FF. The improved FF in these devices is attributed to lower series resistance as calculated from the slope of the current density vs. voltage plot of the devices. 1:1:1 devices show the best performance attributed to the highest J_{sc} and V_{oc} . The enhanced FF in 1:1:1 and 1:0.5:1 devices is attributed mainly to the significantly improved shunt resistance (R_{sh}). The 1:2:1 devices showed a poor R_{sh} of $134.8 \Omega \text{ cm}^2$ compared to $7017.5 \Omega \text{ cm}^2$ and 3506.3 for the 1:0.5:1 and 1:1:1 devices respectively. The lower shunt resistance is attributed to current leakage which could possibly arise from poor morphology (pinholes, cracks *etc.*). The role of scan direction had a minimal impact on the photovoltaic parameters for devices processed from all three precursor ratios (see the ESI,† Fig. S1 and Table S1). The negligible hysteresis observed can be attributed to surface defect passivation by the fullerene (C_{60}) layer as commonly observed in inverted perovskite solar cells.¹⁹ The difference in current densities is also confirmed by external quantum efficiency (EQE) spectra as shown in Fig. 2b. The negligible shift in the onset of EQE was observed in all devices as supported by the similar onset of the UV-visible absorption spectra (see the ESI,† Fig. S3). 1:1:1 devices show the highest EQE in the absorption range of the active layer. While 1:2:1 devices showed the lowest EQE with a constant decrease in the entire absorption regime, 1:0.5:1 devices show comparatively higher EQE at lower wavelengths and lower EQE at higher wavelengths. Higher EQE is attributed to higher charge collection in the devices in 1:1:1 solar cells. Specifically, the improvement in EQE at longer wavelengths can be attributed to enhanced charge extraction at the back interface in 1:1:1 devices.²⁰ Although the integrated J_{sc} values from the EQE measurements follow the same trend as the device parameters shown in Fig. 2a, a $\sim 10\%$ offset was observed which could be due to the spectral mismatch or shadow mask induced changes in the device area. It is also critical to understand the variation in photovoltaic parameters with the thickness which can reveal the quality of the active layers. The change in photovoltaic parameters vs. thickness is plotted in Fig. 2c. Different active layer thicknesses were obtained by varying the spin coating speed of the precursor solution. For 1:2:1 devices, it is clearly seen that as the active layer thickness increases from ~ 300 nm to ~ 600 nm the PCE and FF decrease. The decrease in the FF is attributed to the higher series resistance of the solar cells. The optimal thickness of the active layer was found to be 300–400 nm resulting in a maximum PCE of $\sim 9.5\%$ for devices with 1:2:1 precursor ratios. In contrast, devices derived from 1:1:1 and 1:0.5:1 precursor ratios showed the opposite trend, *i.e.*, with an increasing active layer thickness the PCE improved. The improvement in PCE with

Table 1 Photovoltaic parameters of perovskite solar cells derived from different precursor ratios

Precursor ratio ($\text{PbI}_2:\text{MAAc}:\text{MAI}$)	V_{oc} (mV)	J_{sc} (mA cm^{-2})	FF (%)	PCE (%)	R_s ($\Omega \text{ cm}^2$)	R_{sh} ($\Omega \text{ cm}^2$)
1:0.5:1	847	18.29	75.69	11.74	5.12	7017.5
1:1:1	1002	21.66	69.10	15.00	7.35	3506.3
1:2:1	856	16.31	58.08	8.11	11.66	134.8

the higher thickness in 1:1:1 devices is due to enhanced J_{sc} indicative of higher absorption and improved charge collection. The FF in 1:1:1 and 1:0.5:1 devices was fairly constant with increasing thickness indicative of a better quality perovskite film having lower series resistance and leakage current. The optimal thickness for the highest PCE was found to be 400–500 nm for 1:1:1 and 1:0.5:1 devices. From these thickness dependent photovoltaic parameter trends, it can be concluded that the charge transport in 1:1:1 and 1:0.5:1 devices is superior to transport in 1:2:1 devices. We also evaluated the photovoltaic properties of devices fabricated with a 1:1.5:1 precursor ratio (Fig. S2 and Table S1 in ESI†). The 1:1.5:1 devices showed an improved photovoltaic performance when compared to 1:2:1 devices, while still being inferior to equimolar 1:1:1 devices.

To correlate the differences in thickness and precursor ratio dependent photovoltaic behavior with the surface morphology and cross sectional field effect, scanning electron microscopy (FESEM) was performed. Fig. 3 shows the FESEM images of the top view and cross section of perovskite films prepared using different ratios of precursor materials MAI, MAAC, and PbI_2 . Fig. 3a–c represent the top view and Fig. 3d–f represent the cross sectional view of 1:0.5:1, 1:1:1 and 1:2:1 films respectively. It is clearly evident that the precursor ratio has a significant impact on the grain size, distribution, morphology and surface roughness of the perovskite films. It is seen from the surface SEM images that for all ratios mostly polygon shaped grains of size ranging from 100–500 nm formed the film. A film coated with pure PbI_2 and MAI shows a very rough morphology with several cracks and incomplete coverage as observed previously (Fig. S4 in the ESI†).⁵ The surface morphology of the 1:1.5:1 films was also imaged (Fig. S5 in the ESI†), and the grain sizes were found to be in between the sizes observed for 1:2:1 and 1:1:1 films. Thus the precursor ratio plays a critical role in determining the surface morphology and specifically the grain

sizes. Obviously, in terms of regularity and uniformity of grains, a 1:1:1 precursor ratio results in the best film. Although the top view images show tightly packed grains and a continuous film for all ratios, the cross sectional images show many irregularities especially for 1:0.5:1 and 1:2:1 ratios. Grains are also laterally very uniform and large for the 1:1:1 ratio compared to the other two ratios. A rougher surface was observed for films derived from the 1:0.5:1 precursor ratio whereas smoother flat surfaces were noticed for 1:2:1 and 1:1:1 films. Due to the formation of possible single crystalline grains along the thickness, the photovoltaic efficiency is less dependent on the active layer thickness for the 1:1:1 ratio. Such single crystalline grains were also observed for perovskite films grown by a two step method where the authors exposed the as deposited perovskite films to air prior to thermal annealing.²¹ While the route of perovskite deposition is different, we observe the same effect where perovskite crystallization occurs during spin deposition. This crystallization acts as a template for continuous grain growth along the thickness as observed in both 1:0.5:1 and 1:1:1 films. The morphology of 1:2:1 is similar to the morphology reported for perovskite films derived from the 3:1 MAI: $Pb(Ac)_2$ precursor.²² Along the same lines, since the 1:2:1 ratio shows many grains and grain boundaries along the thickness, the photovoltaic efficiency decreases with thicker active layer films. Due to the higher density of trap states at the grain boundaries, charge transport is severely hindered leading to higher series resistance and thereby lowering the FF in 1:2:1 devices. At this point, it is important to emphasize that the different precursor ratios only affect the phase composition which in turn drives the nucleation and grain growth during film deposition. While the phase components for each ratio remain the same before and after annealing, the kinetics of perovskite nucleation seems to be the determining factor for the final film morphology. It is also important to note that, unlike DMSO, PbI_2 does not form mono or bi adducts with MAAC as observed in several other reports.^{2,23} These reports also emphasize that monoadducts are ideal for the formation of higher quality grains, however, the key difference is that the change in the precursor ratio in our case only affects the nucleation rather than the formation of different adducts or phases. Hence, the 1:1:1 precursor ratio aids in the formation of perovskite phase seeds which serve as a template for the growth of single crystalline grains along the thickness. Similar perovskite crystallization is also observed during the spin coating process of the 1:0.5:1 film but at the cost of a rougher morphology. While the MAAC byproduct is essential to obtain a smoother morphology, crystallization during spin coating governs the growth mechanism, which in turn determines the final grain size of perovskite films. Hence, the critical reason for high efficiency in devices with lower MAAC ratios is attributed to the differences in the final film morphology determined by the perovskite nucleation and growth mechanism.

To study the grain structure induced changes in carrier density and lifetime, photoluminescence (PL) measurements were performed. Fig. 4a shows the integrated PL spectra of perovskite films derived from 1:0.5:1, 1:1:1 and 1:2:1

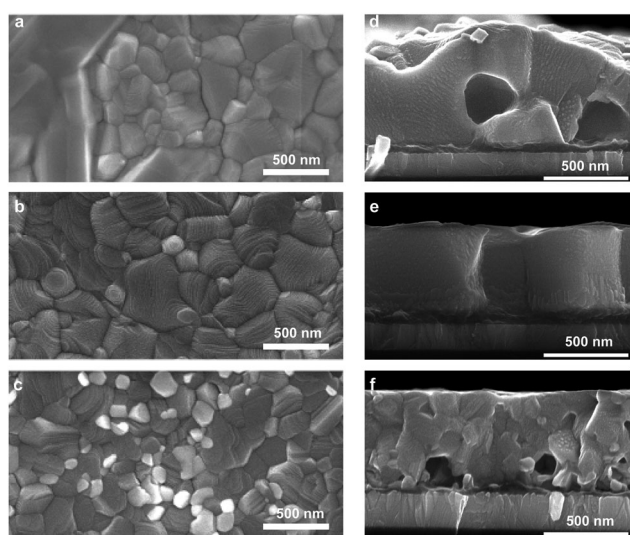


Fig. 3 Top view (a–c) and cross sectional (d–f) scanning electron microscopy (SEM) of (a and d) 1:0.5:1, (b and e) 1:1:1 and (c and f) 1:2:1 films. The scale bars in each figure represent 500 nm.

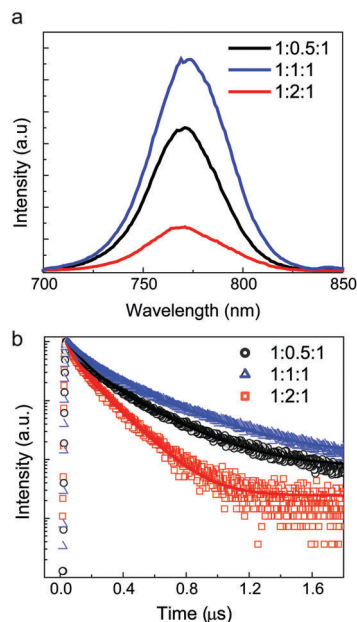


Fig. 4 (a) Integrated photoluminescence and (b) time resolved photoluminescence (symbols represent data and lines represent bi-exponential fit) of annealed perovskite films derived from different mixing ratios.

precursor mixing ratios. With the same excitation, the PL intensity obtained for the films derived from 1:1:1 and 1:0.5:1 precursor ratios is much higher than that for the 1:2:1 films. The enhanced PL in the 1:1:1 films is indicative of lower trap assisted (non-radiative) and higher band-to-band (radiative) recombination. Thus the 1:2:1 films have lower PL intensity due to the higher density of trap states, which leads to higher trap assisted recombination. As seen in the SEM images, 1:2:1 samples have smaller grains and a higher density of grain boundaries which act as non-radiative recombination centers.²⁴ The trend in peak PL intensity is in line with the J_{sc} trend observed in photovoltaic devices. Furthermore, time resolved photoluminescence (TRPL) measurements were performed to evaluate the carrier lifetime in these films. The TRPL data were fit with the second order exponential decay equation to find the fast recombination (τ_1) and slow recombination (τ_2) lifetimes. Previous reports of TRPL studies on perovskite films have shown that the fast decay is due to the surface and grain boundary defects and slow decay arises from bulk defects within the grain interiors.^{25,26} The 1:2:1 films showed $\tau_1 = 46$ ns and $\tau_2 = 165$ ns. In contrast, 1:1:1 and 1:0.5:1 films showed a much higher lifetime compared to 1:2:1 films. The τ_1 times were 94 ns and 96 ns and the τ_2 times were found to be 293 ns and 361 ns for the 1:0.5:1 and 1:1:1 films respectively. Higher carrier lifetimes for 1:1:1 and 1:0.5:1 films indicate slower trap assisted recombination kinetics than that for the film derived from the 1:2:1 precursor ratio. Similar fast decay dynamics for 1:0.5:1 and 1:1:1 films indicated lower surface and grain boundary defects in the films consistent with the SEM analysis. The highest τ_1 and τ_2 lifetimes in 1:1:1 films indicated superior radiative recombination kinetics due to the suppressed surface and bulk defect density. Furthermore, the comparable lifetimes

of 1:0.5:1 films with 1:1:1 films indicate that a relatively lower V_{oc} observed in 1:0.5:1 devices could be due to the higher bulk recombination in 1:0.5:1 derived perovskite films.²⁷ However, the origin of the high FF in 1:0.5:1 films is still not clear and needs further investigation.

To ensure the compatibility of the discussed one step method for other halides, we fabricated perovskite light emitting diodes (PeLED) with $\text{CH}_3\text{NH}_3\text{PbBr}_3$ as an emissive layer. Bromide based perovskites have shown to be promising for light emission due to their higher exciton binding energy compared to other halide based perovskites.^{26,28} The device structure of PeLEDs is shown in Fig. 5a. PEDOT:PSS and BPhen/LiF were used as hole and electron injection layers respectively. The emissive layers were coated in a similar manner to that of the iodide based perovskite thin films with PbBr_2 :MAAc:MABr molar ratios of 1:2:1 and 1:1:1. Unlike the iodide based perovskites, bromide based perovskite films coated with the 1:0.5:1 ratio possessed a very rough morphology and showed no electroluminescence and hence were not considered for comparison. The photographs of Fig. 5a show the emission of PeLEDs from 1:1:1 and 1:2:1 ratios when biased at 5 V. It is clearly seen that 1:1:1 PeLEDs show a much brighter and intense emission of green light. The emission of both devices corresponded to a wavelength of 519 nm and had a full width half maximum of 20 nm (see the ESI,† Fig. S6). Fig. 5b shows the current density–voltage–luminance (J – V – L) plots of PeLEDs fabricated with 1:1:1 and 1:2:1 precursor ratios. Both devices show a diode behavior with a turn on voltage of ~ 4.5 V. While the current density values are similar, 1:1:1 devices show an order of magnitude higher luminance than the 1:2:1 PeLED device. Similar to the iodide based films, higher luminance in 1:1:1 devices could

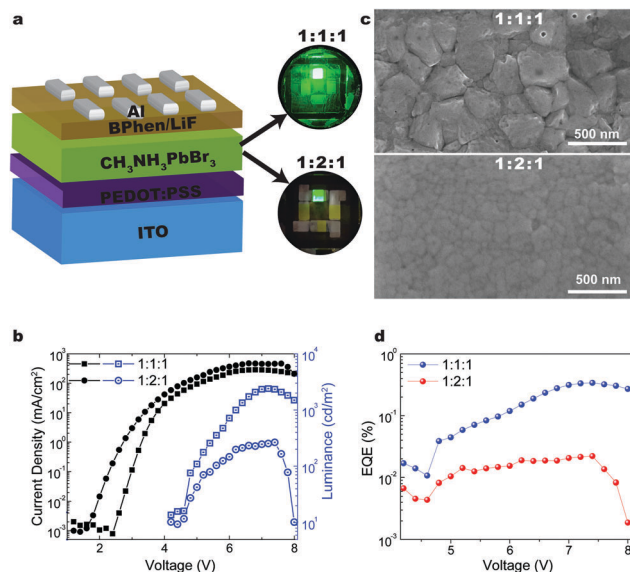


Fig. 5 (a) Device schematic of perovskite light emitting diodes (PeLEDs) with photographs of working PeLEDs at 5 V bias, (b) a current density–voltage–luminance plot, (c) scanning electron microscopic images and (d) external quantum efficiency vs. input voltage of PeLEDs derived from different mixing ratios. Scale bar in SEM images represents 500 nm.

be attributed to higher band-to-band radiative recombination. The lower luminance for 1:2:1 devices, on the other hand, can be due to higher trap induced recombination. The higher traps are attributed to higher defective regions such as grain boundaries as observed in FESEM images shown in Fig. 5c. The 1:1:1 films showed larger grains (300–500 nm) compared to the 1:2:1 films which have grain sizes ranging from 50–100 nm. Due to the presence of smaller grains and a higher density of grain boundaries, trap assisted recombination is more dominant in 1:2:1 devices. Hence as seen in Fig. 5d the EQEs of 1:1:1 devices were an order magnitude higher than those of 1:2:1 devices. The maximum EQEs obtained were 0.02% and 0.34% at 7.4 V for 1:2:1 and 1:1:1 devices respectively. While the relative changes in the device results were remarkable, the observed performance is still lower than the recent literature reported values. The observed photovoltaic and luminous efficiencies can be improved further by process optimization,²⁹ interface engineering³⁰ and appropriate halide/cation doping.³¹ Using this facile method of film deposition and growth, we anticipate that future efforts will be extended to other mixed cation and halide perovskites for efficient optoelectronic devices.

Conclusion

In conclusion, MAAc based perovskite synthesis is a single step, scalable and reproducible technique for efficient optoelectronic device fabrication compared to current techniques in practice. Table S2 in the ESI† lists the reported performances of solar cells for different synthesis techniques of perovskites with a generic architecture “transparent electrode/PEDOT:PSS/perovskite/ETL/metal electrode” which is similar to our cell architecture. Evidently, the MAAc precursor based perovskite solar cell exhibits superior performance to the PbAc₂ and PbCl₂ precursor based counterparts. However, two step deposition and hot casted perovskite devices are shown to have better performance at the expense of additional complexity. The two-step perovskite deposition method requires an additional processing step and more optimization parameters. On the other hand, hot casting requires maintenance of both the solution and substrate temperature at the desired point for the optimum film, which is unsuitable for scalable reproduction. The MAAc based synthesis technique ensure simplicity of the process with a high-quality film. From the effect of precursor ratios (1:0.5:1, 1:1:1 and 1:2:1 of PbI₂:MAAc:MAI) on the growth of perovskite films and optoelectronic performances, it was found that the films derived from a higher MAAc ratio (1:2:1) consisted of a precursor intermediate phase predominantly. When the MAAc ratio was equimolar or lower than the PbI₂ molar ratio (1:1:1 and 1:0.5:1), nucleation and crystallization of the perovskite phase occurred during spinning. Photovoltaic devices fabricated with 1:1:1 and 1:0.5:1 precursor ratios showed enhanced power conversion efficiency compared to 1:2:1 devices. With increasing thickness, 1:1:1 devices showed a higher photovoltaic performance, and the opposite was observed for 1:2:1 devices. This opposite trend in photovoltaic performance with thickness was evident

from the change in morphology. SEM images of 1:1:1 and 1:0.5:1 films showed the formation of larger and single crystalline grains along the thickness and smaller grains with higher grain boundaries were observed for 1:2:1 films. Steady state and time resolved photoluminescence spectroscopy showed higher radiative recombination and lifetime for perovskite films derived from the 1:1:1 precursor ratio than other ratios indicating lower defect density than the films derived from other ratios.

Perovskite based LEDs have potential as a less expensive alternative to current commercially available III-Nitride based LEDs. The fabrication process, material cost, fabrication facility and choice of a suitable substrate make state of the art III-Nitride based LEDs more expensive.^{32–34} Therefore, we have also investigated the equimolar methylammonium acetate route compatibility with bromide based perovskites for electroluminescent devices. Similar to the photovoltaic trend, perovskite LEDs fabricated from the equimolar (1:1:1) precursor ratio showed enhanced electrical to optical performance compared to devices processed from the 1:2:1 ratio. Detailed comparative discussion of the PeLEDs and the state of the art commercial LEDs is provided in the ESI.† This study provides insight into the critical parameters of the growth mechanism for large perovskite grains with a smooth and compact morphology. Furthermore, it also shows strong potential for scalability due to the facile deposition technique for a large scale and high throughput coating process.

Experimental section

Synthesis of methylammonium acetate

Methylammonium acetate (MAAc) was synthesized by reacting anhydrous methylammonium (MA) gas with acetic acid and quenching the salt in toluene. MA gas was evolved when NaOH was added to the aqueous solution of MA and was passed through an NaOH column into a flask containing 5 ml glacial acetic acid in toluene. MAAc precipitated in the toluene was decanted and dried under vacuum overnight and stored in N₂ for further use.

Preparation of perovskite precursor solutions. PbI₂ (Sigma Aldrich), MAAc and MAI (Lumtec) were mixed in different molar ratios (1:2:1, 1:1:1 and 1:0.5:1) in DMF (1 M). 1:2:1 and 1:1:1 precursor solution ratios were also achieved by mixing Pb(Ac)₂, PbI₂ and MAI when mixed in 1:0:3 and 0.5:0.5:2 molar ratios in DMF respectively. The solutions were filtered with a 1 μm PTFE filter prior to coating.

Solar cell fabrication

Pre-cut and pre-patterned ITO glass substrates were cleaned by ultrasonication using Deconex OP121 detergent and deionized water. The substrates were dried, O₂ plasma treated for 7 minutes, and then coated with PEDOT:PSS (Clevios™ P VP AI 4083) to form a 35 nm thick layer. The substrates were then transferred into a N₂ glove box having <1 ppm of O₂ and H₂O. The precursor solutions were then spun cast on top of the ITO/PEDOT:PSS substrates at different speeds to attain different thicknesses. After coating the perovskite layers, the substrates

were transferred to a fume hood and annealed at 100 °C for 5 minutes in air (R.H. ~ 35–45%). The annealed perovskite layers were then transferred to an evaporation chamber for the deposition of 40 nm C₆₀, 8 nm of BCP and 100 nm of Al sequentially using a shadow mask. The active area of the devices was calculated to be 6.25 mm² from the overlap of the ITO and Al electrodes.

Light emitting diode fabrication

Pre-cut and pre-patterned ITO glass substrates, and samples were cleaned as described before and coated with PEDOT:PSS. The precursor solutions composed of 1 : 1 : 1 and 1 : 2 : 1 molar ratios of PbBr₂ : MAAc : MABr were spun coated at 3000 rpm to achieve a 200 nm thick layer. The substrates were then annealed at 60 °C for 60 min in air (R.H. ~ 35–45%). Following the annealing process, the perovskite substrates were transferred to the evaporation chamber for the deposition of 40 nm of BPhen, 7.5 nm of LiF, and 100 nm of Al sequentially using a shadow mask.

Device characterization

Perovskite solar cells were illuminated with an Oriel ABA solar simulator and current–voltage characteristics were obtained using a Keithley 2400 sourcemeter. The xenon lamp intensity was set to AM 1.5G, 100 mW cm⁻² using a NIST calibrated photodiode. Devices were scanned from -0.2 V to 1.2 V (forward) and 1.2 V to -0.2 V (reverse) at a scan rate of 0.11 V s⁻¹. Current density–voltage–luminance readings of the PeLEDs were recorded using an Agilent Technologies U3606B sourcemeter and a Gamma Scientific Model 2500 integrating sphere coupled to a Thor Labs PDA100A Si amplified photodetector. A PR-650 SpectraScan colorimeter was used for calibration.

Film characterization

UV-Visible absorption spectra were recorded using a Shimadzu UV-2501 spectrophotometer. ITO/PEDOT:PSS substrates were used as the reference for all the films. Absorption spectra of the films were recorded from 900 nm to 200 nm wavelengths respectively. FESEM imaging was performed using an FEI Helios NanoLab 400. A probe current of 5.4 pA was used for imaging all samples at an accelerating voltage of 5 kV. XRD measurements were performed using a Rigaku SmartLab diffractometer. XRD patterns were obtained using a parallel beam configuration on the perovskite films. To avoid conversion due to ambient exposure, all films were coated with a thin layer of PMMA in a glove box prior to XRD characterization. Integrated photoluminescence (PL) and time-resolved photoluminescence (TRPL) measurements were performed with a 430 nm excitation wavelength. The excitation system (Spectra Physics) was composed of a frequency-doubled neodymium vanadate laser pumping a mode-locked Ti:sapphire laser to produce ~150 fs broad pulses at a wavelength of 860 nm with a repetition rate of 80 MHz. Pulse frequency was then chosen using a pulse selector. A second harmonic generator then produces the desired 430 nm excitation wavelength. The PL signal is recorded and passed to a spectrometer with 0.64 m

focal length equipped with a fast micro-channel plate photo-multiplier tube. The TRPL decay curves are obtained at the emission wavelength (760 nm) using time-correlated single photon counting calibrated to span a 2 ns measurement range. The instrument response of the TRPL system was ~2 ns. The laser spot size at the samples is ~100 μm. FTIR spectra were recorded using a Nicolet 6700 spectrometer in ATR mode. The optical cavity was constantly purged with N₂ while recording the FTIR spectra. Background scans were run prior to recording each sample's FTIR spectrum.

Conflicts of interest

There are no conflicts to declare.

Acknowledgements

This work was supported by ACS Petroleum Research Fund #56095-UNI6 (Program Manager Askar Fahr), NSF Grant #1040035 (Program Manager Guebre X. Tessema), and the U.S. Department of Defense W911NF-16-1-0518 (Program Officer Paul Armistead).

Notes and references

- Z. Xiao, C. Bi, Y. Shao, Q. Dong, Q. Wang, Y. Yuan, C. Wang, Y. Gao and J. Huang, *Energy Environ. Sci.*, 2014, 7, 2619.
- Z. Xiao, Q. Dong, C. Bi, Y. Shao, Y. Yuan and J. Huang, *Adv. Mater.*, 2014, 26, 6503–6509.
- W. S. Yang, J. H. Noh, N. J. Jeon, Y. C. Kim, S. Ryu, J. Seo and S. Il Seok, *Science*, 2015, 348, 1234–1237.
- J. W. Lee, H. S. Kim and N. G. Park, *Acc. Chem. Res.*, 2016, 49, 311–319.
- N. J. Jeon, J. H. Noh, Y. C. Kim, W. S. Yang, S. Ryu and S. Il Seok, *Nat. Mater.*, 2014, 13, 1–7.
- F. Huang, Y. Dkhissi, W. Huang, M. Xiao, I. Benesperi, S. Rubanov, Y. Zhu, X. Lin, L. Jiang, Y. Zhou, A. Gray-Weale, J. Etheridge, C. R. McNeill, R. A. Caruso, U. Bach, L. Spiccia and Y. B. Cheng, *Nano Energy*, 2014, 10, 10–18.
- B. Conings, A. Babayigit, M. T. Klug, S. Bai, N. Gauquelin, N. Sakai, J. T.-W. Wang, J. Verbeeck, H.-G. Boyen and H. J. Snaith, *Adv. Mater.*, 2016, 1–9.
- N. K. Noel, S. N. Habisreutinger, B. Wenger, M. T. Klug, M. T. Hörantner, M. B. Johnston, R. J. Nicholas, D. T. Moore and H. Snaith, *Energy Environ. Sci.*, 2016, 10, 145–152.
- W. Qiu, T. Merckx, M. Jaysankar, C. Masse de la Huerta, L. Rakocevic, W. Zhang, U. W. Paetzold, R. Gehlhaar, L. Froyen, J. Poortmans, D. Cheyons, H. J. Snaith and P. Heremans, *Energy Environ. Sci.*, 2016, 9, 484–489.
- D. Forgács, M. Sessolo, H. J. Bolink, Y. C. Kim, S. Ryu, J. Seo, S. I. Seok, S. Lu, Y. Liu, H. Zhou, Y. Yang, S. Yao, Y. Chen, R. H. Friend, L. A. Estroff, U. Wiesner and H. J. Snaith, *J. Mater. Chem. A*, 2015, 3, 14121–14125.
- W. Zhang, M. Saliba, D. T. Moore, S. K. Pathak, M. T. Horantner, T. Stergiopoulos, S. D. Stranks, G. E. Eperon, J. A. Alexander-Webber, A. Abate, A. Sadhanala, S. Yao, Y. Chen, R. H. Friend,

- L. A. Estroff, U. Wiesner and H. J. Snaith, *Nat. Commun.*, 2015, **6**, 6142.
- 12 F. K. Aldibaja, L. Badia, E. Mas-Marzá, R. S. Sánchez, E. M. Barea and I. Mora-Sero, *J. Mater. Chem. A*, 2015, **3**, 9194–9200.
- 13 D. T. Moore, H. Sai, K. W. Tan, D. M. Smilgies, W. Zhang, H. J. Snaith, U. Wiesner and L. A. Estroff, *J. Am. Chem. Soc.*, 2015, **137**, 2350–2358.
- 14 L. Zhao, D. Luo, J. Wu, Q. Hu, W. Zhang, K. Chen, T. Liu, Y. Liu, Y. Zhang, F. Liu, T. P. Russell, H. J. Snaith, R. Zhu and Q. Gong, *Adv. Funct. Mater.*, 2016, **26**, 3551.
- 15 J. Qing, H. T. Chandran, Y. H. Cheng, X. K. Liu, H. W. Li, S. W. Tsang, M. F. Lo and C. S. Lee, *ACS Appl. Mater. Interfaces*, 2015, **7**, 23110–23116.
- 16 S. Venkatesan, F. Hao, J. Kim, Y. Rong, Z. Zhu and Y. Liang, *Nano Res.*, 2017, **10**, 1413–1422.
- 17 A. Dubey, N. Kantack, N. Adhikari, K. M. Reza, S. Venkatesan, M. Kumar, D. Khatiwada, S. Darling and Q. Qiao, *J. Mater. Chem. A*, 2016, **4**, 10231–10240.
- 18 D. Bi, C. Yi, J. Luo, J.-D. Décoppet, F. Zhang, S. M. Zakeeruddin, X. Li, A. Hagfeldt and M. Grätzel, *Nat. Energy*, 2016, **1**, 16142.
- 19 G. E. Eperon, V. M. Burlakov, P. Docampo, A. Goriely and H. J. Snaith, *Adv. Funct. Mater.*, 2014, **24**, 151–157.
- 20 K. G. Stamplecoskie, J. S. Manser and P. V. Kamat, *Energy Environ. Sci.*, 2015, **8**, 208–215.
- 21 J. S. Manser, B. Reid and P. V. Kamat, *J. Phys. Chem. C*, 2015, **119**, 17065–17073.
- 22 Z. Song, S. C. Wathage, A. B. Phillips, B. L. Tompkins, R. J. Ellingson and M. J. Heben, *Chem. Mater.*, 2015, **27**, 4612–4619.
- 23 X. Chen, H. Cao, H. Yu, H. Zhu, H. Zhou, L. Yang and S. Yin, *J. Mater. Chem. A*, 2016, **4**, 9124–9132.
- 24 Z. Zhu, V. G. Hadjiev, Y. Rong, R. Guo, B. Cao, Z. Tang, F. Qin, Y. Li, Y. Wang, F. Hao, S. Venkatesan, W. Li, S. Baldelli, A. M. Guloy, H. Fang, Y. Hu, Y. Yao, Z. Wang and J. Bao, *Chem. Mater.*, 2016, **28**, 7385–7393.
- 25 T. Oku, *Sol. Cells*, 2015, 77–101.
- 26 S.-S. Li, C.-H. Chang, Y.-C. Wang, C.-W. Lin, D.-Y. Wang, J.-C. Lin, C.-C. Chen, H.-S. Sheu, H.-C. Chia, W.-R. Wu, U.-S. Jeng, C.-T. Liang, R. Sankar, F.-C. Chou and C.-W. Chen, *Energy Environ. Sci.*, 2016, **9**, 1282–1289.
- 27 Y. Shao, Z. Xiao, C. Bi, Y. Yuan and J. Huang, *Nat. Commun.*, 2014, **5**, 1–7.
- 28 M. Yang, T. Zhang, P. Schulz, Z. Li, G. Li, D. H. Kim, N. Guo, J. J. Berry, K. Zhu and Y. Zhao, *Nat. Commun.*, 2016, **7**, 2–10.
- 29 B. Yang, O. Dyck, J. Poplawsky, J. Keum, A. Poretzky, S. Das, I. Ivanov, C. Rouleau, G. Duscher, D. Geohegan and K. Xiao, *J. Am. Chem. Soc.*, 2015, **137**, 9210–9213.
- 30 L. Oesinghaus, J. Schlipf, N. Giesbrecht, L. Song, Y. Hu, T. Bein, P. Docampo and P. Müller-Buschbaum, *Adv. Mater. Interfaces*, 2016, **3**, 1600403.
- 31 J. Cao, X. Jing, J. Yan, C. Hu, R. Chen, J. Yin, J. Li and N. Zheng, *J. Am. Chem. Soc.*, 2016, **138**, 9919–9926.
- 32 G. Li, W. Wang, W. Yang and Y. Lin, *Rep. Prog. Phys.*, 2016, **79**, 56501.
- 33 H. Masui, S. Nakamura, S. P. DenBaars and U. K. Mishra, *IEEE Trans. Electron Devices*, 2010, **57**, 88–100.
- 34 W. Wang, H. Wang, W. Yang and Y. Zhu, *Sci. Rep.*, 2016, **6**, 24448.